PHYSICS

Quasiparticle interference evidence of the topological Fermi arc states in chiral fermionic semimetal CoSi

Qian-Qian Yuan[1,2]*, Liqin Zhou[3,4]*, Zhi-Cheng Rao[3,4], Shangjie Tian[5], Wei-Min Zhao[1,2], Cheng-Long Xue[1,2], Yixuan Liu[5], Tiantian Zhang[3,4], Cen-Yao Tang[3,4], Zhi-Qiang Shi[1,2], Zhen-Yu Jia[1,2], Hongming Weng[3,6,7†], Hong Ding[3,6], Yu-Jie Sun[3,6,7†], Hechang Lei[5], Shao-Chun Li[1,2†]

Chiral fermions in solid state feature "Fermi arc" states, connecting the surface projections of the bulk chiral nodes. The surface Fermi arc is a signature of nontrivial bulk topology. Unconventional chiral fermions with an extensive Fermi arc traversing the whole Brillouin zone have been theoretically proposed in CoSi. Here, we use scanning tunneling microscopy/spectroscopy to investigate quasiparticle interference at various terminations of a CoSi single crystal. The observed surface states exhibit chiral fermion–originated characteristics. These reside on (001) and (011) but not (111) surfaces with π-rotation symmetry, spiral with energy, and disperse in a wide energy range from ~−200 to ~+400 mV. Owing to the high-energy and high-space resolution, a spin-orbit coupling–induced splitting of up to ~80 mV is identified. Our observations are corroborated by density functional theory and provide strong evidence that CoSi hosts the unconventional chiral fermions and the extensive Fermi arc states.

INTRODUCTION

Recently, great progress has been achieved in condensed matter physics in search of the analog of the elementary particles, as described in high-energy physics. The three types of fundamental fermions—Dirac, Weyl, and Majorana—have been found in solids in the form of low-energy fermionic excitations near the topologically or symmetrically protected band crossing (*1*–*17*). Because these fermionic excitations are constrained by the crystalline symmetry much lower than the Poincaré symmetry in high-energy physics, new types of fermions that have no high-energy counterparts have also been proposed and found in condensed matter materials (*18*–*30*), including spin-3/2 Rarita-Schwinger-Weyl (RSW) excitations (*26*, *27*), threefold nexus fermions (*22*, *24*), spin-1 Weyl fermions (*28*), double Weyl fermions (*29*), double Dirac fermions (*30*), etc. These unconventional chiral fermions may exhibit fantastic physical properties, such as helical surface states (*31*, *32*), unusual magnetotransport (*33*–*35*), the circular photogalvanic effect (*36*, *37*), etc.

The chiral crystalline family of transition metal silicides, including CoSi, RhSi, RhGe, and CoGe, has been recently proposed as ideal candidates to host unconventional chiral fermion quasiparticles through ab initio calculations (*38*–*40*). They are expected to have a number of advantages against the previously explored Weyl semimetals. For example, multiple types of topological chiral nodes coexist and are located close to the Fermi energy; there is no trivial band crossing the Fermi energy, and the transport properties are expectedly dominated by the chiral fermions (*38*, *39*); as protected by the nonsymmorphic crystalline symmetry and time-reversal symmetry, the Fermi arc is rather extensive, in contrast to the short ones reported in previous Weyl semimetals (*7*–*12*). These extraordinary chiral fermions in CoSi family are the spin-1 Weyl fermions of threefold degeneracy and the double Weyl fermions of fourfold degeneracy when spin-orbit coupling (SOC) is ignored in a spinless case. If SOC is considered, then the above spin-1 Weyl fermion evolves into a spin-3/2 RSW fermion of fourfold degeneracy (with spin degree of freedom), and the double Weyl fermion becomes a double spin-1 Weyl fermion of sixfold degeneracy (again with spin degree of freedom) (*38*, *39*). In the absence of symmetry constraint, these chiral nodes in CoSi family are not necessary to be of equal energy, and in a wide energy window, one can, in principle, observe the Fermi arc states. Bulk band structure and surface states of CoSi have been characterized by angle-resolved photoemission spectroscopy (ARPES) (*41*–*44*). However, a full understanding of the exotic surface Fermi arc is still lacking, which plays an indispensable role in the determination of the bulk topology and nontrivial properties. In this work, we systematically investigated the surfaces of a CoSi single crystal by using a high-resolution scanning tunneling microscopy (STM)/scanning tunneling spectroscopy (STS) technique and proved the surface Fermi arc states through quasiparticle interference (QPI) measurement, which is corroborated by density functional theory (DFT) simulation.

[1]National Laboratory of Solid State Microstructures, School of Physics, Nanjing University, Nanjing 210093, China. [2]Collaborative Innovation Center of Advanced Microstructures, Nanjing University, Nanjing 210093, China. [3]Beijing National Laboratory for Condensed Matter Physics and Institute of Physics, Chinese Academy of Sciences, Beijing 100190, China. [4]University of Chinese Academy of Sciences, Beijing 100049, China. [5]Department of Physics and Beijing Key Laboratory of Optoelectronic Functional Materials and Micro-Nano Devices, Renmin University of China, Beijing 100872, China. [6]CAS Center for Excellence in Topological Quantum Computation, University of Chinese Academy of Sciences, Beijing 100190, China. [7]Songshan Lake Materials Laboratory, Dongguan, Guangdong 523808, China.
*These authors contributed equally to this work.
†Corresponding author. Email: scli@nju.edu.cn (S.-C.L.); yjsun@iphy.ac.cn (Y.-J.S.); hmweng@iphy.ac.cn (H.W.)

RESULTS AND DISCUSSION

The crystal structure of CoSi belongs to the nonsymmorphic space group $P2_13$ (no. 198) with the lattice constant of $a = b = c = 4.45$ Å (*45*), as illustrated in Fig. 1A. The unit cell of CoSi contains four Co and four Si atoms, with each Co (Si) atom covalently bonded to six nearest neighboring Si (Co) atoms. In the Co (Si)–terminated (001) surface, the Co (Si) atom and the underlying Si (Co) atom located outside the center form a zigzag atomic chain. The reciprocal Brillouin zone (BZ) of CoSi is sketched in Fig. 1B, where the time-reversal invariant momenta are marked. The projected surfaces crossing the

Γ point for (001), (011), and (111) are highlighted in different colors. DFT calculation indicates that the bulk energy band of CoSi contains high-fold degenerate crossings at Γ and *R*, as shown in Fig. 1C. The band crossing at Γ point forms the spin-3/2 RSW fermion node of fourfold degeneracy, and that at *R* point forms the double spin-1 Weyl node of sixfold degeneracy. The two types of chiral fermions are illustrated in Fig. 1D. Because of the no-go theorem, the RSW fermion node carries the chiral charge of +4, and the double spin-1 Weyl fermion carries the chiral charge of −4. Therefore, if Γ/*R* points are projected to different momenta at the surface BZ, for instance, $\bar{\Gamma}/\bar{\mathrm{M}}$ on the (001) and $\bar{\Gamma}/\bar{\mathrm{X}}$ on the (011) surfaces as illustrated in Fig. 1 (E and F), then extensive Fermi arcs are formed as the chiral conducting states between them. The inclusion of SOC leads to the doubling of the Fermi arcs. However, in the case of the (111) surface, the Γ and *R* points are projected to the same momentum at the center of the surface BZ, and their opposite Chern numbers of ±4 thus overlap with each other. As a result, the topologically protected Fermi arc from the surface states connecting the two opposite chiral nodes is not observable, as illustrated in Fig. 1G.

Atomically flat surfaces of various terminations of CoSi single crystals can be achieved after cycles of argon ion sputtering and annealing in ultrahigh vacuum. Figure 2A shows, for example, the STM topographic image of the (001) surface. The step height, as shown in the inset of Fig. 2A, is measured to be ~4.5 Å, consistent with the lattice constant along the [001] direction. The step height of ~2.25 Å is also occasionally observable, which corresponds to the distance between two adjacent atomic planes, i.e., half size of the unit cell (see fig. S1). The high-resolution STM image in Fig. 2B displays the square lattice of a = 4.45 Å. The zigzag chain structure formed by Co—Si bonding, as shown in the inset of Fig. 2B, further confirms that the exposed surface is (001) oriented. The other two surfaces of (011) and (111) are also geometrically confirmed, as shown in Fig. 2 (C and D) and fig. S1. The atomically resolved images displayed in Fig. 2C show the rectangle lattice of a = 4.45 Å and b = 6.27 Å for the (011) surface and, in Fig. 2D, the hexagonal lattice of a = 6.27 Å for the (111) surface.

Differential conductance (dI/dV) spectrum [reflecting the local density of state (LDOS)] taken on the (001) surface of CoSi shows the nonvanishing states in the whole bias range of ±0.2 V, indicating the (semi-)metallic nature, as shown in Fig. 2E. Intriguingly, the LDOS exhibits a singular peak near the Fermi energy. It is generally believed that either the flat dispersion of a bulk band or the surface states can result in an enhancement in LDOS. To figure out the origin of this singular peak, we took the dI/dV measurement on the (011) and (111) surfaces as well for comparison, as shown together in Fig. 2E and fig. S2. One can see that the dI/dV spectra taken on the (011) and (001) surfaces are obviously distinct from that on the (111) surface. The former two display similar LDOS peaks near the Fermi energy, but in the latter, the intensity of the peak is completely suppressed. According to previous DFT calculation and ARPES measurement (*38*, *39*, *41*–*44*), the flat bulk band is projected to all the three surfaces. However, as illustrated in Fig. 1, there exist only surface Fermi arc states on the (001) and (011) surfaces and no such surface states on the (111) surface. Therefore, we deduced that the LDOS peak observed on the (001) and (011) surfaces is most likely related to the presence of the topological surface Fermi arc states. To further manifest it, the LDOS including/excluding the surface states is calculated for the projected surfaces, as displayed in Fig. 2F.

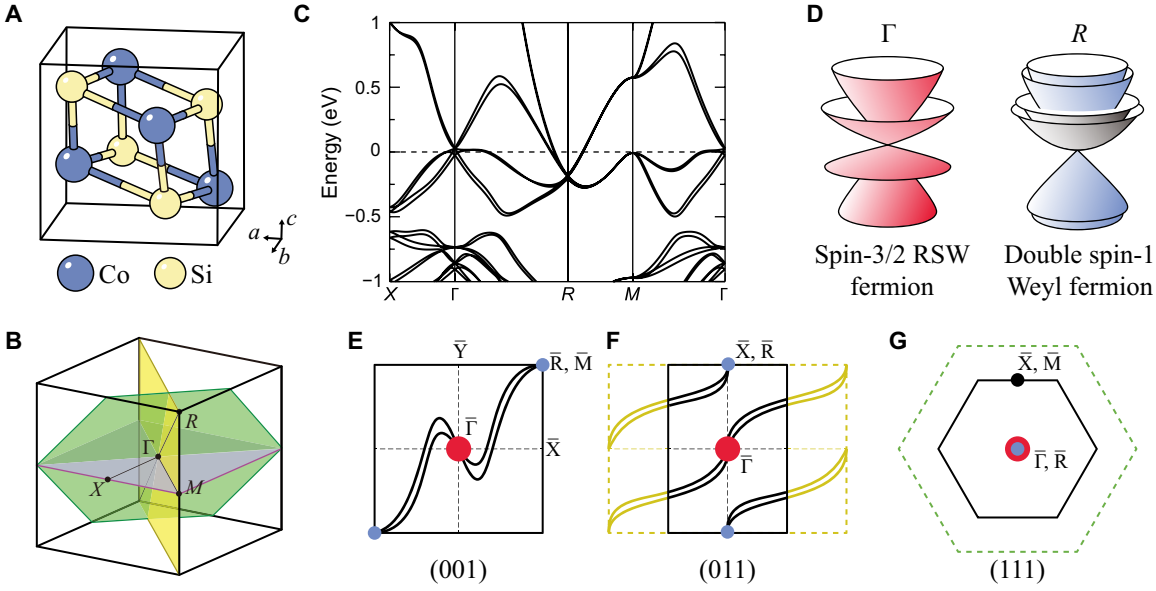

Fig. 1. Crystal structure and electronic structure of CoSi single crystals. (**A**) Lattice structure of CoSi ($a = b = c$ = 4.45 Å). The blue and yellow balls represent Co and Si atoms, respectively. (**B**) Reciprocal BZ of CoSi. Γ, *X*, *M*, and *R* points are high-symmetry positions of the bulk BZ. The purple, yellow, and green planes indicate the projected surface crossing at Γ for the (001), (011), and (111) orientation, respectively. (**C**) DFT-calculated bulk band structure with SOC along high-symmetry directions. (**D**) Schematic illustration of the fourfold degenerated spin-3/2 RSW fermion node at the Γ point and the sixfold degenerated double spin-1 Weyl nodes at the *R* point. (**E** to **G**) Schematic illustrations of the surface BZs and Fermi arcs for the (001), (011), and (111) surfaces. The colored dashed lines in (F) and (G) represent the projected surfaces as shown in (D). The red and blue solid dots indicate the surface projections of Γ and *R* points, respectively. They are located at $\bar{\Gamma}$ and $\bar{\mathrm{M}}$ position for the (001) surface and $\bar{\Gamma}$ and $\bar{\mathrm{X}}$ positions for the (011) surface as displayed in (E) and (F). The black arcs schematically show the surface Fermi arcs connecting the projections of bulk chiral nodes. Γ and *R* are projected to the same $\bar{\Gamma}$ point on the (111) surface.

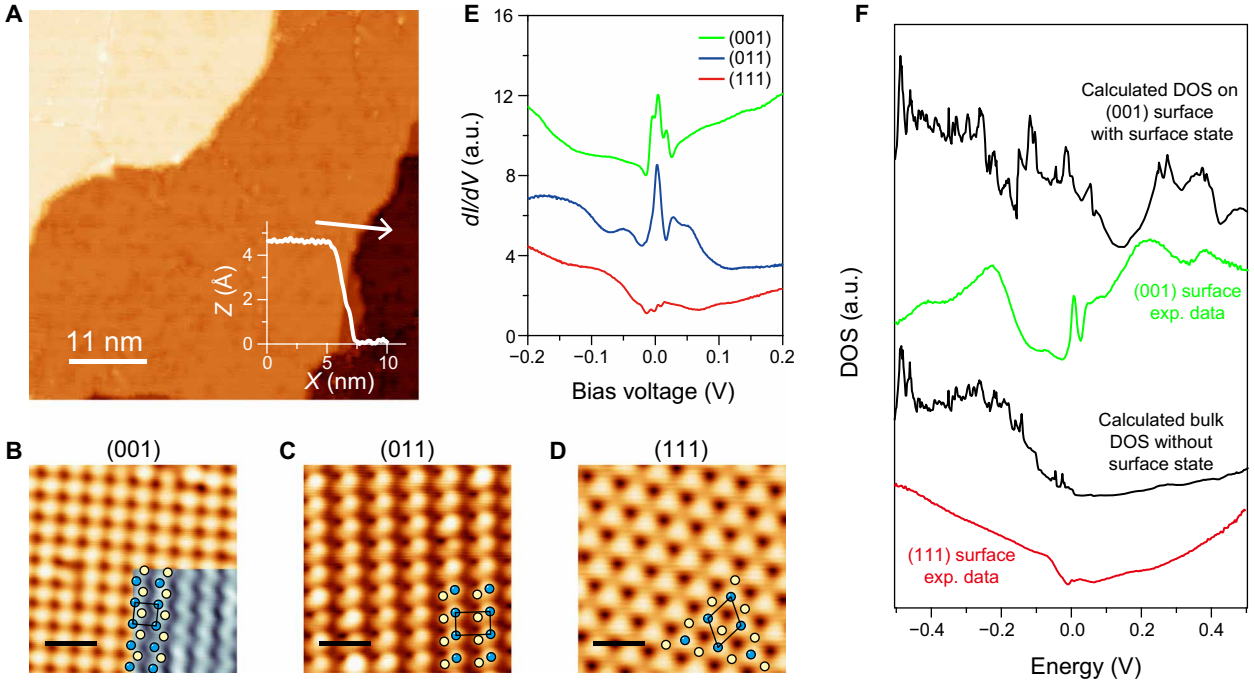

Fig. 2. STM/STS characterization of CoSi surfaces. (**A**) Large-scale STM topographic image (55 nm by 55 nm, $U = 2$ V, $I_t = 50$ pA) of the CoSi (001) surface. Inset: Line-scan profile measured along the white arrowed line, the step height is measured to be ~4.5 Å. (**B**) High-resolution STM image (4 nm by 4 nm, $U = 500$ mV, $I_t = 100$ pA) taken on the (001) surface. Inset: STM image ($U = 60$ mV, $I_t = 1$ nA) showing the zigzag atomic structure. (**C**) High-resolution STM image (4 nm by 4 nm, $U = -100$ mV, $I_t = 500$ pA) of the (011) surface. (**D**) High-resolution STM topography (4 nm by 4 nm, $U = -500$ mV, $I_t = 100$ pA) taken on the (111) surface. The corresponding unit cells are also indicated by the square, the rectangle, and the parallelogram. The blue and yellow dots mark the Co and Si atoms, respectively. Scale bars, 8 Å (B to D). (**E**) Small-range *dI*/*dV* spectra taken on the three surfaces of CoSi. The green, blue, and red curves represent the *dI*/*dV* spectrum for (001), (011), and (111), respectively. a.u., arbitrary units. (**F**) DFT-calculated (001) projected surface DOS (up black) and experimentally measured *dI*/*dV* curve on the (001) surface (green), calculated bulk DOS without surface states (down black), and measured *dI*/*dV* curve on the (111) surface (red).

There is no prominent peak feature near the Fermi energy in the bulk states. However, the prominent feature due to the existence of the surface states on the (001) surface qualitatively agrees with the measured *dI*/*dV* spectra. It is noteworthy that the *dI*/*dV* spectrum taken on the (111) surface is in good agreement with the calculated LDOS without surface states, as shown in Fig. 2F.

QPI measurements were carried out at the three surfaces of (001), (011), and (111) to further characterize the surface Fermi arc states. The QPI patterns, as derived from the fast Fourier transform (FFT) of *dI*/*dV* maps measured in real space, can reveal the wave vectors of the electron's elastic scattering and thus the dispersive information of the electron bands. It has been widely used in manifesting the existence of topological surface states in topological insulators and semimetals (*46*–*50*). The FFT-STS maps taken on the (001) surface are shown in Fig. 3 (A and B). More information can be found in fig. S3. Extensive features can be recognized near the Fermi energy. As marked in Fig. 3A, four prominent eye-shaped features (yellow arrows) are located at the corners of the first BZ, and two crescent moon–shaped features (black arrows) reside near the Bragg points. These features are beyond the scattering between bulk electron (hole) pockets as usually expected of compact pockets in QPI, as shown in Fig. 3 (E and F). It is obvious that these extensive features do not appear equivalently around the four orthogonal Bragg peaks (or along the orthogonal high-symmetry directions) and without mirror symmetry but exist with π-rotation symmetry, suggesting that the patterns are likely from the chiral surface states.

To quantitatively understand the origin of the scattering channels, we performed DFT-generated QPI simulation. Both QPI simulations for the (001) surface including and excluding surface states are presented in Fig. 3 (C and D as well as E and F, respectively). Unexpectedly, similar eye-shaped patterns in the simulation including surface states are also identified, which mainly resulted from the scattering channel of q_1 between surface Fermi arc states, as marked in Fig. 3G. The scattering channel q_2 between surface states leads to a pattern similar to the crescent moon. In addition, the calculated feature is also of π-rotation symmetry, in agreement with the experimental observation. It is noteworthy that the Fermi arc contour depends sensitively on the real atomic geometry of the surface. The QPI pattern may look different as well if the spin texture of the Fermi arc is considered. In any case, the qualitative consistency between experiment and simulation undoubtedly reveals the existence of surface Fermi arc states. Instead, bulk state–associated QPI features, i.e., the expected pocket-like patterns as illustrated in Fig. 3 (E and F), are not well distinguishable, which may be due to either the weak scattering of the three-dimensional–like bulk states or being overwhelmed by the surface state scattering. The presence of surface Fermi arc states is also supported by the QPI data taken on the (011) and (111) surfaces. Figure 3 (I and L) shows the QPI results taken on the (011) and (111) surfaces, and Fig. 3 (J, K, M, and N) shows the corresponding QPI simulations and calculated constant energy contours. More *dI*/*dV* maps taken on the (011) and (111) surfaces can be found in figs. S4 to S7 and movie S1. As marked in Fig. 3I for the (011) surface, the

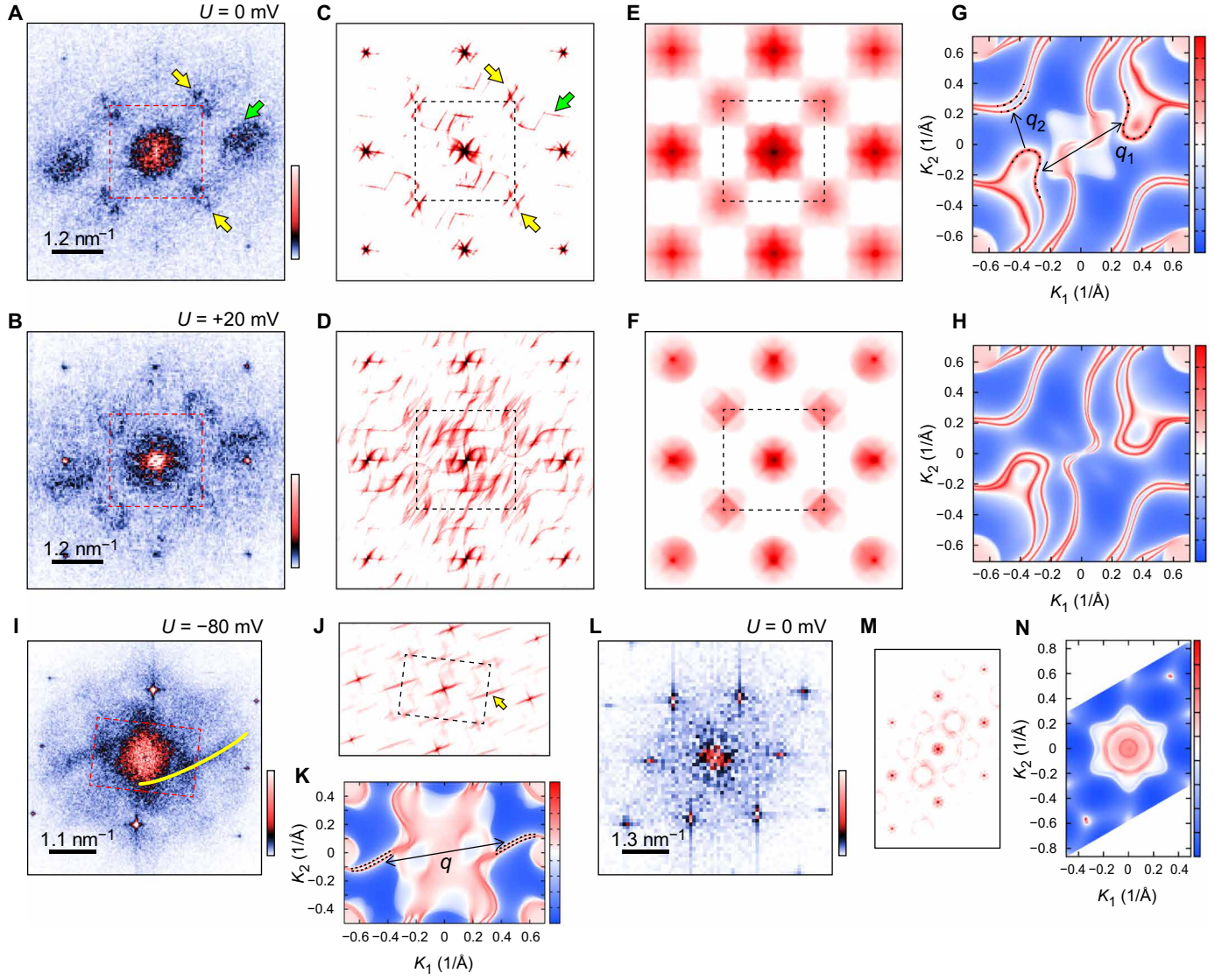

Fig. 3. QPI patterns on various surfaces of CoSi. (**A** and **B**) FFT images transformed from the *dI*/*dV* maps taken on the (001) surface over an area of 25 nm by 21 nm at 0 and +20 mV. U = +60 mV, I = 200 pA; modulation: 12 mV. The yellow arrows indicate the eye-shaped feature, and the green arrow indicates the crescent moon–like pattern around the Bragg peak. The red dashed square marks the surface first BZ. (**C** and **D**) QPI simulations including SOC that are generated from both the surface states and the bulk states at E_F (Fermi energy) and E_F + 20 mV for (001). There exist two kinds of prominent interference patterns as marked by yellow and green arrows. The black dashed squares mark the first surface BZ, the same as in (A) and (B). (**E** and **F**) Calculated QPI simulation by removing the surface states part from (C) and (D) for the (001) surface at E_F and E_F + 20 mV, respectively. (**G** and **H**) Calculated constant energy contours at E_F and E_F + 20 mV of the (001) surface with Fermi arcs traversing the whole BZ. The black arrows in (G) indicate the corresponding scattering processes of two kinds of prominent QPI patterns in (C). (**I**) FFT image transformed from the *dI*/*dV* map taken on the (011) surface (U = −80 mV, I_t = 100 pA; modulation: 13 mV) over an area of 40 nm by 40 nm. The red rectangle marks the first BZ of the (011) surface, and the yellow arc highlights the arc-shaped feature. (**J**) QPI simulation including SOC and surface states at −80 mV for the (011) surface. The black dashed rectangle marks the first surface BZ. The yellow arrow indicates the corresponding QPI feature as in (I). (**K**) Calculated constant energy contour for the (011) surface at −80 mV. (**L**) FFT image transformed from the *dI*/*dV* map taken on the (111) surface at 0 mV (U = −60 mV, I_t = 200 pA; modulation: 12 mV) over an area of 10 nm by 10 nm. (**M**) QPI simulation including SOC and surface states at E_F for (111). (**N**) Calculated constant energy contour for the (111) surface at E_F.

arc-shaped feature can be observed connecting two Bragg points and shows π-rotation symmetry. This arc-shaped feature can be reproduced in the corresponding simulated QPI (Fig. 3J), which is associated with the scattering between the topological surface states as marked by the black dashed lines in Fig. 3K. However, no similar extensive feature is observed on the (111) surface, as shown in Fig. 3 (L to N).

There exists a qualitative consistency between QPI measurement and DFT simulation at energies explored, as shown in Fig. 3. Detailed analysis of energy-dependent QPI data reveals that these features, such as the crescent moon–shaped and eye-shaped, spiral anticlockwise around the Γ point gradually as energy increases, as shown in figs. S8 and S9 and movie S2. The "Fermi arc" state, as observed on the (011) surface, shows a similar anticlockwise rotation around

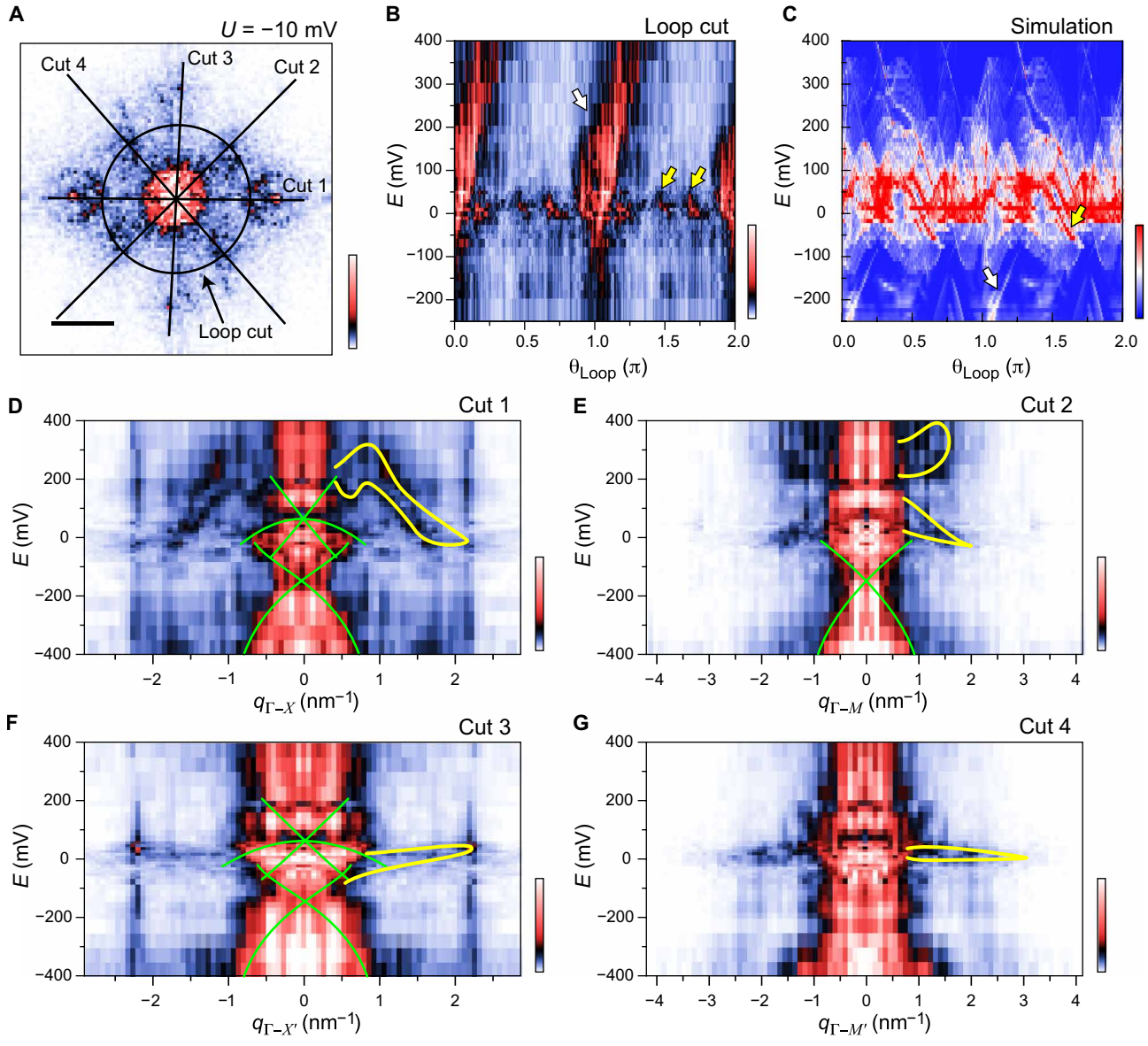

Fig. 4. Energy dispersion of surface states with chirality. (**A**) Experimental FFT image ($U = -10$ mV) transformed from the *dI*/*dV* map taken on the (001) surface. Scale bar, 1.4 nm^{-1}. The black straight line cuts (1 to 4) indicate the four high-symmetry directions $\bar{\Gamma}$-$\bar{X}$, $\bar{\Gamma}$-$\bar{X}'$, $\bar{\Gamma}$-$\bar{M}$, and $\bar{\Gamma}$-$\bar{M}'$. (**B**) *E*-*q* dispersion extracted along the loop cut as marked by the black circle in (A). The magnitude of the scattering wave vector ($|\vec{q}|$) along the loop is $3\pi/2a$. The θ_{Loop} is rotated anticlockwise and relative to the cut 1. The yellow arrows mark the right chirality of the QPI features along cut 2, cut 3, and cut 4, and the white arrow marks the left chirality of the QPI features along cut 1. (**C**) Calculated *E*-*q* dispersion along the loop ($|\vec{q}| = 3\pi/2a$) based on a series of surface states–based QPI simulations. The yellow and white arrows mark the right and left chiral features, respectively. (**D** to **G**) *E*-*q* dispersions along $\bar{\Gamma}$-$\bar{X}$, $\bar{\Gamma}$-$\bar{X}'$, $\bar{\Gamma}$-$\bar{M}$, and $\bar{\Gamma}$-$\bar{M}'$ as marked in (A) extracted from the energy-dependent QPI maps. The green guiding lines indicate two Dirac-like band crossings. These two Dirac nodes are located at ~+50 and −150 mV. The additional extensive dispersions of the surface Fermi arcs are marked by yellow lines.

the Γ point as energy increases, as shown in fig. S5 and movie S1. This is a strong evidence of the Fermi arc's winding around the chiral node, as predicted by DFT (*38*, *39*).

In the following, we investigated the winding property of the Fermi arc states in detail. Qualitatively, the QPI pattern turns anticlockwise as energy increases. We took a loop cut along the circle, as illustrated in Fig. 4A, and depicted the energy-dependent profiles in Fig. 4B. The QPI dispersive features, as marked by yellow and white arrows, go up to cross the Fermi energy with chirality. Such chirality can be qualitatively reproduced in the DFT-generated simulation, as shown in Fig. 4C. We emphasize that, although the QPI dispersion does not straightforwardly give the band structure, the chirality observed can be surely ascribed to the chirality of the surface Fermi arc states.

Quantitative *E*-*q* dispersions of the surface Fermi arc states along high symmetric directions of $\bar{\Gamma}$-$\bar{X}$, $\bar{\Gamma}$-$\bar{X}'$, $\bar{\Gamma}$-$\bar{M}$, and $\bar{\Gamma}$-$\bar{M}'$, as marked in Fig. 4A, are also extracted and depicted in Fig. 4 (D to G). The feature near the center is rather complicated, which should include

the mix of multi intra–bulk band scattering at Γ and *R* and the small vectors from Fermi arc states. Although identifying the scattering channels is difficult, two Dirac-like band crossings are distinguishable along the specific directions. One of them can be recognized along $\overline{\Gamma}$-$\overline{X}$ and $\overline{\Gamma}$-$\overline{X}'$, located near ~+50 mV, and another along $\overline{\Gamma}$-$\overline{X}'$ and $\overline{\Gamma}$-M, located at ~−150 mV, as particularly outlined by the green lines in Fig. 4 (E and F). They can be assigned to the projected chiral nodes at Γ and *R*, respectively, the energies of which are consistent with the recent ARPES measurement (*41*, *42*, *44*). Apart from this, the surface Fermi arc states contribute to the additional dispersive curves as guided by the yellow lines in Fig. 4 (D to G). These yellow lines indicate that the QPI feature appears as a pair, and each of the pair evolves in a similar way, except for an energy shift. On the other hand, at the presence of SOC, one surface state splits into two branches, and thus, one would expect to observe the paired QPI features originating from these SOC split surface states, considering the spin-conserving process. Considering such consistency between the experiment and the SOC split surface states, we believe that the observed paired QPI feature comes from the SOC splitting. The value of SOC splitting varies with momentum and energy. According to Fig. 4, we estimate that the maximum may be up to ~80 mV at ~+200 mV, in agreement with the DFT calculation (*39*). However, the SOC splitting near the Fermi energy is relatively smaller, in the range between ~25 and ~35 mV. Such a SOC-induced Fermi arc splitting is not observed in recent ARPES studies (*41*–*44*), possibly because of the limit of energy resolution. The surface Fermi arc dispersion also shows strong anisotropy along different directions, as shown in Fig. 4 (D to G), fig. S10, and movie S2, which is originated from the anisotropic contours of the Fermi arcs. The total energy window that the surface Fermi arc spans is estimated as ~600 mV (from −200 to +400 mV), also consistent with the theoretical expectation.

CONCLUSIONS

In summary, through the FFT-STS measurement, we have undoubtedly demonstrated the topological Fermi arc states on the (001) and (011) surfaces of CoSi single crystals. The observed QPI patterns from these Fermi arcs are consistent with the simulation, which confirms that CoSi hosts the chiral spin-3/2 RSW fermion and double spin-1 Weyl fermions. The chiral surface states exhibit a number of exotic properties, such as the intensity singularity in LDOS, large SOC splitting, wide energy window, etc. Further exploration is expected to find novel physics associated with the surface Fermi arc states.

MATERIALS AND METHODS

Sample preparation

CoSi single crystals were grown by a chemical vapor transport method. Co and Si powders in 1:1 molar ratio were added into a silica tube with a length of 200 mm and an inner diameter of 14 mm. Then, 200-mg I_2 was added into the tube as a transport reagent. The single CoSi crystals with an average size of ~2 mm were obtained. Because of the cubic structure and strong covalent bonding, it was difficult to obtain a perfect surface by cleaving single CoSi crystals. So, we cut and polished the single crystals before loading into ultrahigh vacuum, and then, the samples were in situ repeatedly Ar^+ ion–sputtered and annealed until clear-reflection high-energy electron diffraction patterns appeared.

STM and STS characterization

The STM characterization was performed in a commercial STM system (USM-1500, UNISOKU) at 4.2 K. The base pressure was less than 1×10^{-10} torr. The STM topographic images were collected under a constant current mode with a mechanically polished Pt-Ir tip. The *dI*/*dV* spectra were acquired with a lock-in amplifier technique.

DFT calculations

The calculation based on the DFT to simulate the electronic structure of CoSi was performed by using the VASP (Vienna Ab initio Simulation Package) package (*51*), with the generalized gradient approximation in Perdew-Burke-Ernzerhof form (*52*) as the exchange-correlation functional. The cutoff of energy was set to 450 eV, and the BZ integration was performed on a 10 by 10 by 10 mesh. SOC was taken into account for all calculations. We built a 10-U cell-thick slab to obtain the projected surface LDOS, with a 16-Å-thick vacuum layer along the (001) direction to eliminate the interaction between slabs. To investigate the surface states and QPI, a tight-binding model was constructed by the *d* orbits of Co and *p* orbits of Si based on the maximally localized Wannier functions (*53*). The surface states and QPI were calculated by the WannierTools package (*54*).

SUPPLEMENTARY MATERIALS

Supplementary material for this article is available at http://advances.sciencemag.org/cgi/content/full/5/12/eaaw9485/DC1

Determination of the various surface of single CoSi crystals
LDOS peaks observed in the *dI*/*dV* curves on the (001) and (011) surfaces
Measured QPI patterns on various terminations
Fig. S1. Structural characterization for various terminations of a single CoSi crystal.
Fig. S2. Spatially resolved *dI*/*dV* spectra taken on various terminations of a single CoSi crystal.
Fig. S3. Energy-dependent QPI patterns for the CoSi (001) surface (data I).
Fig. S4. Real-space *dI*/*dV* maps taken on the CoSi (011) surface.
Fig. S5. Energy-dependent QPI patterns for the CoSi (011) surface.
Fig. S6. Real-space *dI*/*dV* maps taken on the CoSi (111) surface.
Fig. S7. Energy-dependent QPI patterns for the CoSi (111) surface.
Fig. S8. Real-space *dI*/*dV* maps taken on the CoSi (001) surface (data II).
Fig. S9. Energy-dependent QPI patterns for the CoSi (001) surface (data II).
Fig. S10. Energy dispersions in different directions.
Movie S1. Energy-dependent QPI patterns for the CoSi (011) surface.
Movie S2. Energy-dependent QPI patterns for the CoSi (001) surface.

REFERENCES AND NOTES

1. Z. Wang, Y. Sun, X.-Q. Chen, C. Franchini, G. Xu, H. Weng, X. Dai, Z. Fang, Dirac semimetal and topological phase transitions in A_3Bi (A=Na, K, Rb). *Phys. Rev. B* **85**, 195320 (2012).
2. S. M. Young, S. Zaheer, J. C. Y. Teo, C. L. Kane, E. J. Mele, A. M. Rappe, Dirac semimetal in three dimensions. *Phys. Rev. Lett.* **108**, 140405 (2012).
3. Z. Wang, H. Weng, Q. Wu, X. Dai, Z. Fang, Three-dimensional Dirac semimetal and quantum transport in Cd_3As_2. *Phys. Rev. B* **88**, 125427 (2013).
4. Z. K. Liu, J. Jiang, B. Zhou, Z. J. Wang, Y. Zhang, H. M. Weng, D. Prabhakaran, S.-K. Mo, H. Peng, P. Dudin, T. Kim, M. Hoesch, Z. Fang, X. Dai, Z. X. Shen, D. L. Feng, Z. Hussain, Y. L. Chen, A stable three-dimensional topological Dirac semimetal Cd_3As_2. *Nat. Mater.* **13**, 677–681 (2014).
5. Z. K. Liu, B. Zhou, Y. Zhang, Z. J. Wang, H. M. Weng, D. Prabhakaran, S.-K. Mo, Z. X. Shen, Z. Fang, X. Dai, Z. Hussain, Y. L. Chen, Discovery of a three-dimensional topological Dirac semimetal, Na_3Bi. *Science* **343**, 864–867 (2014).
6. S.-Y. Xu, C. Liu, S. K. Kushwaha, R. Sankar, J. W. Krizan, I. Belopolski, M. Neupane, G. Bian, N. Alidoust, T.-R. Chang, H.-T. Jeng, C.-Y. Huang, W.-F. Tsai, H. Lin, P. P. Shibayev, F.-C. Chou, R. J. Cava, M. Z. Hasan, Observation of Fermi arc surface states in a topological metal. *Science* **347**, 294–298 (2015).
7. H. Weng, C. Fang, Z. Fang, B. A. Bernevig, X. Dai, Weyl semimetal phase in noncentrosymmetric transition-metal monophosphides. *Phys. Rev. X* **5**, 011029 (2015).

8. B. Q. Lv, H. M. Weng, B. B. Fu, X. P. Wang, H. Miao, J. Ma, P. Richard, X. C. Huang, L. X. Zhao, G. F. Chen, Z. Fang, X. Dai, T. Qian, H. Ding, Experimental Discovery of Weyl Semimetal TaAs. *Phys. Rev. X* **5**, 031013 (2015).
9. S.-Y. Xu, I. Belopolski, N. Alidoust, M. Neupane, G. Bian, C. Zhang, R. Sankar, G. Chang, Z. Yuan, C.-C. Lee, S.-M. Huang, H. Zheng, J. Ma, D. S. Sanchez, B. K. Wang, A. Bansil, F. C. Chou, P. P. Shibayev, H. Lin, S. Jia, M. Z. Hasan, Discovery of a Weyl fermion semimetal and topological Fermi arcs. *Science* **349**, 613–617 (2015).
10. L. X. Yang, Z. K. Liu, Y. Sun, H. Peng, H. F. Yang, T. Zhang, B. Zhou, Y. Zhang, Y. F. Guo, M. Rahn, D. Prabhakaran, Z. Hussain, S.-K. Mo, C. Felser, B. Yan, Y. L. Chen, Weyl semimetal phase in the non-centrosymmetric compound TaAs. *Nat. Phys.* **11**, 728–732 (2015).
11. B. Q. Lv, N. Xu, H. M. Weng, J. Z. Ma, P. Richard, X. C. Huang, L. X. Zhao, G. F. Chen, C. E. Matt, F. Bisti, V. N. Strocov, J. Mesot, Z. Fang, X. Dai, T. Qian, M. Shi, H. Ding, Observation of Weyl nodes in TaAs. *Nat. Phys.* **11**, 724–727 (2015).
12. S.-M. Huang, S.-Y. Xu, I. Belopolski, C.-C. Lee, G. Chang, B. Wang, N. Alidoust, G. Bian, M. Neupane, C. Zhang, S. Jia, A. Bansil, H. Lin, M. Z. Hasan, A Weyl Fermion semimetal with surface Fermi arcs in the transition metal monopnictide TaAs class. *Nat. Commun.* **6**, 7373 (2015).
13. Z. K. Liu, L. X. Yang, Y. Sun, T. Zhang, H. Peng, H. F. Yang, C. Chen, Y. Zhang, Y. F. Guo, D. Prabhakaran, M. Schmidt, Z. Hussain, S.-K. Mo, C. Felser, B. Yan, Y. L. Chen, Evolution of the Fermi surface of Weyl semimetals in the transition metal pnictide family. *Nat. Mater.* **15**, 27–31 (2015).
14. M.-X. Wang, C. Liu, J.-P. Xu, F. Yang, L. Miao, M.-Y. Yao, C. L. Gao, C. Shen, X. Ma, X. Chen, Z.-A. Xu, Y. Liu, S.-C. Zhang, D. Qian, J.-F. Jia, Q.-K. Xue, The coexistence of superconductivity and topological order in the Bi_2Se_3 thin films. *Science* **336**, 52–55 (2012).
15. V. Mourik, K. Zuo, S. M. Frolov, S. R. Plissard, E. P. Bakkers, L. P. Kouwenhoven, Signatures of Majorana fermions in hybrid superconductor-semiconductor nanowire devices. *Science* **336**, 1003–1007 (2012).
16. S. Nadj-Perge, I. K. Drozdov, J. Li, H. Chen, S. Jeon, J. Seo, A. H. MacDonald, B. A. Bernevig, A. Yazdani, Observation of Majorana fermions in ferromagnetic atomic chains on a superconductor. *Science* **346**, 602–607 (2014).
17. Y. Sun, S.-C. Wu, B. H. Yan, Topological surface states and Fermi arcs of the noncentrosymmetric Weyl semimetals TaAs, TaP, NbAs, and NbP. *Phys. Rev. B* **92**, 115428 (2015).
18. A. A. Soluyanov, D. Gresch, Z. Wang, Q. Wu, M. Troyer, X. Dai, B. A. Bernevig, Type-II Weyl semimetals. *Nature* **527**, 495–498 (2015).
19. K. Deng, G. L. Wan, P. Deng, K. N. Zhang, S. J. Ding, E. Y. Wang, M. Z. Yan, H. Q. Huang, H. Y. Zhang, Z. L. Xu, J. Denlinger, A. Fedorov, H. T. Yang, W. H. Duan, H. Yao, Y. Wu, S. S. Fan, H. J. Zhang, X. Chen, S. Y. Zhou, Experimental observation of topological Fermi arcs in type-II Weyl semimetal $MoTe_2$. *Nat. Phys.* **12**, 1105–1110 (2016).
20. L. Huang, T. M. McCormick, M. Ochi, Z. Zhao, M.-T. Suzuki, R. Arita, Y. Wu, D. Mou, H. Cao, J. Yan, N. Trivedi, A. Kaminski, Spectroscopic evidence for a type II Weyl semimetallic state in $MoTe_2$. *Nat. Mater.* **15**, 1155–1160 (2016).
21. T.-R. Chang, S.-Y. Xu, G. Chang, C.-C. Lee, S.-M. Huang, B. Wang, G. Bian, H. Zheng, D. S. Sanchez, I. Belopolski, N. Alidoust, M. Neupane, A. Bansil, H.-T. Jeng, H. Lin, M. Z. Hasan, Prediction of an arc-tunable Weyl Fermion metallic state in $Mo_xW_{1-x}Te_2$. *Nat. Commun.* **7**, 10639 (2016).
22. H. Weng, C. Fang, Z. Fang, X. Dai, Topological semimetals with triply degenerate nodal points in θ-phase tantalum nitride. *Phys. Rev. B* **93**, 241202 (2016).
23. H. M. Weng, C. Fang, Z. Fang, X. Dai, Coexistence of Weyl fermion and massless triply degenerate nodal points. *Phys. Rev. B* **94**, 165201 (2016).
24. Z. Zhu, G. W. Winkler, Q. Wu, J. Li, A. A. Soluyanov, Triple Point Topological Metals. *Phys. Rev. X* **6**, 031003 (2016).
25. B. Q. Lv, Z.-L. Feng, Q. N. Xu, X. Gao, J.-Z. Ma, L.-Y. Kong, P. Richard, Y.-B. Huang, V. N. Strocov, C. Fang, H.-M. Weng, Y.-G. Shi, T. Qian, H. Ding, Observation of three-component fermions in the topological semimetal molybdenum phosphide. *Nature* **546**, 627–631 (2017).
26. M. Ezawa, Pseudospin-$\frac{3}{2}$fermions, type-II Weyl semimetals, and critical Weyl semimetals in tricolor cubic lattices. *Phys. Rev. B* **94**, 195205 (2016).
27. L. Liang, Y. Yu, Semimetal with both Rarita-Schwinger-Weyl and Weyl excitations. *Phys. Rev. B* **93**, 045113 (2016).
28. B. Bradlyn, J. Cano, Z. Wang, M. G. Vergniory, C. Felser, R. J. Cava, B. A. Bernevig, Beyond Dirac and Weyl fermions: Unconventional quasiparticles in conventional crystals. *Science* **353**, aaf5037 (2016).
29. Y. Xu, L.-M. Duan, Type-II Weyl points in three-dimensional cold-atom optical lattices. *Phys. Rev. A* **94**, 053619 (2016).
30. B. J. Wieder, Y. Kim, A. M. Rappe, C. L. Kane, Double Dirac semimetals in three dimensions. *Phys. Rev. Lett.* **116**, 186402 (2016).
31. X. G. Wan, A. M. Turner, A. Vishwanath, S. Y. Savrasov, Topological semimetal and Fermi-arc surface states in the electronic structure of pyrochlore iridates. *Phys. Rev. B* **83**, 205101 (2011).
32. C. Fang, L. Lu, J. Liu, L. Fu, Topological semimetals with helicoid surface states. *Nat. Phys.* **12**, 936–941 (2016).
33. H. B. Nielsen, M. Ninomiya, The Adler-Bell-Jackiw anomaly and Weyl fermions in a crystal. *Phys. Lett. B* **130**, 389–396 (1983).
34. V. Aji, Adler-Bell-Jackiw anomaly in Weyl semimetals: Application to pyrochlore iridates. *Phys. Rev. B* **85**, 241101 (2012).
35. P. Hosur, X. L. Qi, Recent developments in transport phenomena in Weyl semimetals. *Comp. Rend. Phys.* **14**, 857–870 (2013).
36. F. de Juan, A. G. Grushin, T. Morimoto, J. E. Moore, Quantized circular photogalvanic effect in Weyl semimetals. *Nat. Commun.* **8**, 15995 (2017).
37. G. Chang, B. J. Wieder, F. Schindler, D. S. Sanchez, I. Belopolski, S.-M. Huang, B. Singh, D. Wu, T.-R. Chang, T. Neupert, S.-Y. Xu, H. Lin, M. Z. Hasan, Topological quantum properties of chiral crystals. *Nat. Mater.* **17**, 978–985 (2018).
38. G. Chang, S.-Y. Xu, B. J. Wieder, D. S. Sanchez, S.-M. Huang, I. Belopolski, T.-R. Chang, S. Zhang, A. Bansil, H. Lin, M. Z. Hasan, Unconventional Chiral fermions and large topological Fermi arcs in RhSi. *Phys. Rev. Lett.* **119**, 206401 (2017).
39. P. Tang, Q. Zhou, S.-C. Zhang, Multiple types of topological fermions in transition metal silicides. *Phys. Rev. Lett.* **119**, 206402 (2017).
40. T. Zhang, Z. Song, A. Alexandradinata, H. Weng, C. Fang, L. Lu, Z. Fang, Double-Weyl phonons in transition-metal monosilicides. *Phys. Rev. Lett.* **120**, 016401 (2018).
41. D. Takane, Z. Wang, S. Souma, K. Nakayama, T. Nakamura, H. Oinuma, Y. Nakata, H. Iwasawa, C. Cacho, T. Kim, K. Horiba, H. Kumigashira, T. Takahashi, Y. Ando, T. Sato, Observation of Chiral fermions with a large topological charge and associated Fermi-arc surface states in CoSi. arXiv:1809.01312 [cond-mat.mes-hall]. (5 September 2018).
42. D. S. Sanchez, I. Belopolski, T. A. Cochran, X. Xu, J.-X. Yin, G. Chang, W. Xie, K. Manna, V. Süß, C.-Y. Huang, N. Alidoust, D. Multer, S. S. Zhang, N. Shumiya, X. Wang, G.-Q. Wang, T.-R. Chang, C. Felser, S.-Y. Xu, S. Jia, H. Lin, M. Z. Hasan, Discovery of topological chiral crystals with helicoid arc states. arXiv:1812.04466 [cond-mat.mes-hall] (11 December 2018).
43. N. B. M. Schröter, D. Pei, M. G. Vergniory, Y. Sun, K. Manna, F. de Juan, J. A. Krieger, V. Süss, M. Schmidt, P. Dudin, B. Bradlyn, T. K. Kim, T. Schmitt, C. Cacho, C. Felser, V. N. Strocov, Y. Chen, Topological semimetal in a chiral crystal with large chern numbers, multifold band crossings, and long Fermi-arcs. arXiv:1812.03310 [cond-mat.mes-hall] (8 December 2018).
44. Z.-C. Rao, H. Li, T.-T. Zhang, S.-J. Tian, C.-H. Li, B.-B. Fu, C.-Y. Tang, L. Wang, Z.-L. Li, W.-H. Fan, J.-J. Li, Y.-B. Huang, Z.-H. Liu, Y.-W. Long, C. Fang, H.-M. Weng, Y.-G. Shi, H.-C. Lei, Y.-J. Sun, T. Qian, H. Ding, New classes of chiral topological nodes with non-contractible surface Fermi arcs in CoSi. arXiv:1901.03358 [cond-mat.mtrl-sci] (10 January 2019).
45. L. Pauling, A. M. Soldate, The nature of the bonds in the iron silicide, FeSi, and related crystals. *Acta Crystallogr.* **1**, 212–216 (1948).
46. T. Zhang, P. Cheng, X. Chen, J.-F. Jia, X. Ma, K. He, L. Wang, H. Zhang, X. Dai, Z. Fang, X. Xie, Q.-K. Xue, Experimental demonstration of topological surface states protected by time-reversal symmetry. *Phys. Rev. Lett.* **103**, 266803 (2009).
47. P. Roushan, J. Seo, C. V. Parker, Y. S. Hor, D. Hsieh, D. Qian, A. Richardella, M. Z. Hasan, R. J. Cava, A. Yazdani, Topological surface states protected from backscattering by chiral spin texture. *Nature* **460**, 1106–1109 (2009).
48. H. Inoue, A. Gyenis, Z. J. Wang, J. Li, S. W. Oh, S. Jiang, N. Ni, B. A. Bernevig, A. Yazdani, Quasiparticle interference of the Fermi arcs and surface-bulk connectivity of a Weyl semimetal. *Science* **351**, 1184–1187 (2016).
49. H. Zheng, G. Bian, G. Chang, H. Lu, S.-Y. Xu, G. Wang, T.-R. Chang, S. Zhang, I. Belopolski, N. Alidoust, D. S. Sanchez, F. Song, H.-T. Jeng, N. Yao, A. Bansil, S. Jia, H. Lin, M. Z. Hasan, Atomic-scale visualization of quasiparticle interference on a type-II Weyl semimetal surface. *Phys. Rev. Lett.* **117**, 266804 (2016).
50. H. Zheng, S.-Y. Xu, G. Bian, C. Guo, G. Chang, D. S. Sanchez, I. Belopolski, C.-C. Lee, S.-M. Huang, X. Zhang, R. Sankar, N. Alidoust, T.-R. Chang, F. Wu, T. Neupert, F. Chou, H.-T. Jeng, N. Yao, A. Bansil, S. Jia, H. Lin, M. Z. Hasan, Atomic-scale visualization of quantum interference on a Weyl semimetal surface by scanning tunneling microscopy. *ACS Nano* **10**, 1378–1385 (2016).
51. G. Kresse, J. Furthmüller, Efficient iterative schemes for ab initio total-energy calculations using a plane-wave basis set. *Phys. Rev. B Condens. Matter.* **54**, 11169–11186 (1996).
52. J. P. Perdew, K. Burke, M. Ernzerhof, Generalized gradient approximation made simple. *Phys. Rev. Lett.* **77**, 3865–3868 (1996).
53. A. A. Mostofi, J. R. Yates, G. Pizzi, Y. S. Lee, I. Souza, D. Vanderbilt, N. Marzari, An updated version of wannier90: A tool for obtaining maximally-localised Wannier functions. *Comput. Phys. Commun.* **185**, 2309–2310 (2014).
54. Q. S. Wu, S. N. Zhang, H.-F. Song, M. Troyer, A. A. Soluyanov, WannierTools: An open-source software package for novel topological materials. *Comput. Phys. Commun.* **224**, 405–416 (2017).

Acknowledgments
Funding: This work was supported by the National Natural Science Foundation of China (grant nos. 11774149, 11790311, 11574371, 11574394, 11774423, 11822412, and 11674369), the National Key R&D Program of China (grant nos. 2015CB921000, 2016YFA0300504, 2014CB921103, 2016YFA0300600, and 2018YFA0305700), and the Strategic Priority Research Program of Chinese Academy of Sciences (grant no. XDB28000000). L.Z. and H.W. were also supported by the Science Challenge Project (grant no. TZ2016004) and the K. C. Wong Education Foundation (grant no. GJTD-2018-01). **Author contributions:** S.-C.L. conceived the project. Q.-Q.Y. acquired and analyzed the data with the help of W.-M.Z., C.-L.X., Z.-Q.S., and Z.-Y.J. L.Z., T.Z., and H.W. performed the DFT calculations. S.T., Y.L., and H.L. grew the single crystals. Z.-C.R., C.-Y.T., and Y.-J.S. cut and polished the crystals. S.-C.L., H.W., Y.-J.S., H.L., and H.D. discussed the results. Q.-Q.Y. and S.-C.L. wrote the manuscript with contributions from all authors. **Competing interests:** The authors declare that they have no competing interests.

Data and materials availability: All data needed to evaluate the conclusions in the paper are present in the paper and/or the Supplementary Materials. Additional data related to this paper may be requested from the authors.

Submitted 8 February 2019
Accepted 29 October 2019
Published 20 December 2019
10.1126/sciadv.aaw9485

Citation: Q.-Q. Yuan, L. Zhou, Z.-C. Rao, S. Tian, W.-M. Zhao, C.-L. Xue, Y. Liu, T. Zhang, C.-Y. Tang, Z.-Q. Shi, Z.-Y. Jia, H. Weng, H. Ding, Y.-J. Sun, H. Lei, S.-C. Li, Quasiparticle interference evidence of the topological Fermi arc states in chiral fermionic semimetal CoSi. *Sci. Adv.* **5**, eaaw9485 (2019).